Densities of states of substitutional tin and germanium impurities in GaAs, GaP, and InP: Experiment and theory

Jon Wulff Petersen and Axel Svane
Institute of Physics, University of Aarhus, DK-8000 Aarhus C, Denmark

Eugen Holzschuh
Institute of Physics, University of Zürich, CH-8001 Zürich, Switzerland
and the ISOLDE Collaboration, European Organization for Nuclear Research, Geneva, CH-1211 Geneva 23, Switzerland

(Received 7 April 1992; revised manuscript received 17 August 1992)

Measurements of conversion electrons from the outermost valence shell of dilute, substitutional tin and germanium impurity atoms in the III-V semiconductors GaAs, GaP, and InP are described. The measured spectra can be directly related to the local density of states at the probe atoms. The results are compared to theoretical calculations based on the local-density approximation to density-functional theory and using the linear-muffin-tin-orbitals method.

I. INTRODUCTION

The introduction of the various photoelectron spectroscopies such as x-ray photoelectron spectroscopy (XPS), ultraviolet photoelectron spectroscopy (UPS), and others[1] led to a boom in the development of sophisticated theoretical models describing the electronic structure of solids. The results have been used to extract information about the electronic structure of both the surface and the bulk of elementary as well as composite solids. In particular for semiconductors the theoretical models have been further developed to describe systems containing impurities and point defects. In this field, however, the electron spectroscopies cannot be applied and the experimental information has been essentially limited to determinations of symmetries, band-gap levels, and a limited information about the spatial wave-function distribution.[2] It would be highly advantageous to have an experimental method delivering a local information about the electronic structure of a probe atom. This need has been met to some extent by the so-called "nuclear methods," e.g., Mössbauer spectroscopy, perturbed angular correlation, and others.[3] These methods are characterized by the use of a probe nucleus and thus fulfill the criterion of locality. However, the information about the electronic structure of the probe atom is again limited to numbers like the isomer shift and the quadrupole interaction strength. The present paper deals with conversion electron spectroscopy: a method that is able to produce genuine spectroscopic information about the electronic structure of an isolated impurity atom in a solid.

In the internal conversion process of an electromagnetic transition in a nucleus, the transition energy, instead of being emitted as a γ ray, is transferred to an atomic electron. The energy of the ejected electron is smaller by the atomic binding energy than the γ-ray energy. The process takes place at or close to the nucleus. Therefore, the transition probability decreases rapidly when going from the inner towards the outer shells.[4] The conversion electron spectrum thus consists of a series of lines with increasing energies and strongly decreasing intensities. The conversion electrons emerging with the highest energies originate from the valence shells. When analyzed at sufficiently high energy resolution, these electrons deliver a mapping of the occupied electron states. Conversion electron spectroscopy is thus principally similar to the above-mentioned electron spectroscopies, except for the fact that the electron emission process by definition is localized to the atom containing the excited nucleus, i.e., the valence-electron states of the probe atom are studied.

Conversion electron spectroscopy is also conceptually similar to x-ray emission spectroscopy (XES), where x rays, emitted as a core hole is filled by an electron from the valence bands, are energy analyzed.[1] With XES similar—or, in selected cases, better—resolution can be obtained than with electron conversion spectroscopy, but the method is limited to low-Z elements due to lifetime broadening of the core-hole state, and the sensitivity necessary to study dilute impurities has still not been demonstrated in practice.

The principal potential of conversion electron spectroscopy was realized long ago.[5] However, earlier studies were hampered by experimental difficulties: First, rather strong radioactive sources are needed to compensate for the low probability of internal conversion in the valence shells. At the same time, the sources must be thin (a few $\mu g/cm^2$) to limit energy loss of the emitted electrons in the source. Second, a high-luminosity, high-resolution electron spectrometer is needed. The first problem was solved in our case by using ion-implanted sources produced at the ISOLDE on-line mass separator at CERN, Geneva. The second requirement is fulfilled by the Zürich β spectrometer built for a neutrino mass experiment.[6] The usefulness of conversion electron spectroscopy is less restricted than other nuclear methods, since suitable transitions can be identified in some forty elements, most of them having $Z > 30$.

The experimental results are compared to theoretical calculations, which are performed with the "first-principles" linear-muffin-tin-orbital Green's function

method.[7] This method is based on the local-density approximation (LDA) to density-functional theory (DFT), by which complicated exchange and correlation effects are accounted for by a simple local potential entering the one-particle Schrödinger equation. Taken strictly, the DFT only provides the ground-state total energy and charge density of the solid state system considered. There exists no formal connection between the individual one-particle wave functions of DFT and the true quasiparticle amplitudes of the many-electron system, except for the fact that their squares add up to the total charge density. In particular, there is no *a priori* reason to expect the one-particle eigenenergies of DFT to compare with the energies of the true excitations of the solid, which the conversion electron spectroscopy measures. In this work we will follow the widespread practice to relax on this stringency of DFT and in fact compare the calculated LDA density of states for isolated Ge and Sn impurity atoms in III-V semiconductors to the experimental conversion electron spectra. This approach is corroborated by many successes of the LDA eigenvalues in describing fairly accurately the simple excitations of solids, although severe shortcomings of the LDA have also been encountered, (see Ref. 8). One of the most distinct failures of the LDA is its inability to describe the fundamental gaps of semiconductors, which generally are computed 50–100 % too small. In some cases, such as Si, this may be overcome by rigidly shifting the conduction bands upwards (the "scissors operator"), while in other cases, such as Ge, the entire topology of the lowest conduction bands is in error and other procedures must be invoked to repair this.[9] For the present study, this is of minor importance, since we will not focus on the gap region but rather on the valence-band region, the shape of which is generally well described for semiconductors in the LDA.

This paper is organized as follows: Section II contains a short description of the crucial properties of the internal conversion process. Section III contains the experimental details including the data analysis. Section IV gives the details of the theoretical calculations carried out. In Sec. V the experimental results are presented and compared to the calculations and Sec. VI gives our conclusions. Short reports of this work have been published previously.[10,11]

II. INTERNAL CONVERSION

The kinetic energy E_{ce} of conversion electrons ejected from an atomic subshell with quantum numbers n,l can be expressed as

$$E_{ce}=E_N-E_B(n,l)-\phi_{\rm sp}\ , \tag{1}$$

where E_N is the nuclear transition energy and $\phi_{\rm sp}$ is the spectrometer work function. The atomic binding energy $E_B(n,l)$ is measured relative to the Fermi level. By this convention, E_{ce} becomes independent of the sample work function. For inner shells, $E_B(n,l)$ depends on the sample into which the radioactive isotope was implanted. This effect is usually referred to as the chemical shift. It is important to note, however, that the maximum energy is sample independent. This maximum corresponds to electrons from the Fermi level, i.e., with $E_B=0$ by definition, and allows one to define a Fermi energy

$$E_{ce}(F)=E_N-\phi_{\rm sp} \tag{2}$$

in the measured conversion electron spectrum.

The probability of internal conversion $P(M,n,l)$ is a strong function of the multipolarity M of the nuclear transition and of the electron quantum numbers n and l.[4] The intensity distribution of the emitted conversion electrons, $I(E)$, can be written as

$$I(E)=\sum_{n,l} N_{n,l}(E)P(M,n,l)\ , \tag{3}$$

where the total density of states is assumed to be a sum of bands $N_{n,l}(E)$ of well-defined angular momentum character. This is obviously true for the inner shells but turns out to be a good approximation also in many cases for the valence shells, as will be demonstrated in Sec. IV. The conversion coefficients $P(M,n,l)$ are well understood both experimentally and theoretically[4] for the closed shells, but less so for the valence shells. However, ratios of conversion coefficients within a main shell (same n), e.g., $P(M,n,s)/P(M,n,p)$ are essentially independent of the main quantum number n. The conversion electron spectrum is therefore an angular momentum projection of the true density of occupied electron states with known projection coefficients.

III. EXPERIMENTAL PROCEDURE AND DATA ANALYSIS

A. Sample preparation

The radioactive isotopes (^{73}Ga and ^{119}Xe; see Figs. 1 and 2) were obtained from the ISOLDE on-line mass separator[12] as proton-induced spallation-fission products

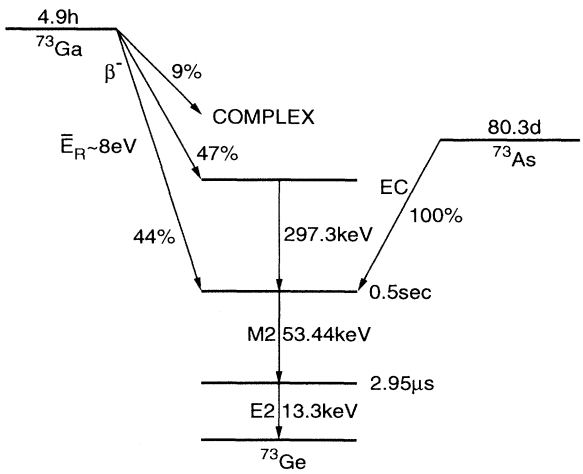

FIG. 1. Decay scheme for the mass 73 isotopes. E_R is the recoil energy transfered to the decaying nucleus. Also given are the lifetimes, the decay modes [electron capture (EC) and β^--decay] and multipolarities ($M2,E2,\ldots$).

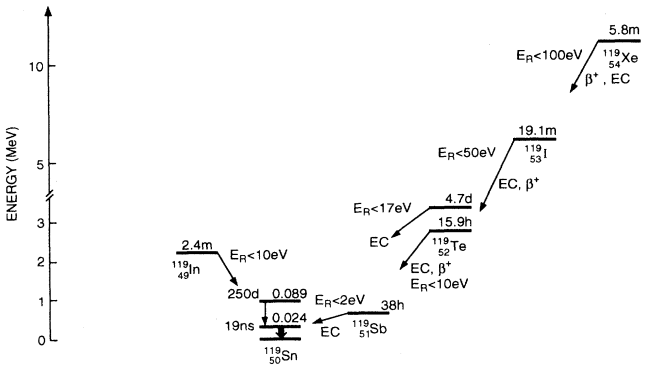

FIG. 2. Decay scheme for the mass 119 isotopes. E_R is the recoil energy transfered to the decaying nucleus. Also given are the lifetimes, the decay modes (EC,β^-, . . .), and multipolarities ($M2$,$E2$, . . .).

from targets (molten lanthanum and uranium carbide, respectively) irradiated by 600-MeV protons from the CERN synchrocyclotron. The radioactivity was evaporated into an ion source, ionized, accelerated to 60 keV, electromagnetically mass separated, and implanted into the substrates under a grazing angle of 5° to the surface. The average depth of the implanted ions was 5–15 nm and the typical source strength, 10^7 to 10^8 decays/s. The total implanted dose ranged from 10^{11} to 10^{13} ions/cm^2, corresponding to a peak concentration of 10^{17} to 10^{19} atoms/cm^3. The substrates were front-polished GaAs, GaP, and InP single crystals. The implanted ^{119}Xe was allowed to decay to ^{119}Sb by waiting for 60 h. The samples were then annealed in a vacuum oven to remove the radiation damage of the implantation process. The temperatures used were chosen to prevent any diffusion of the implanted atoms. The efficiency of the damage removal process and the lattice location of the radioactive isotopes were checked by ^{119}Sn Mössbauer spectroscopy on the ^{119}Sb sources (for details, see Ref. 13). In case of the Ga implantations we relied on results from similar ^{119}Sn Mössbauer spectroscopy results after ^{119}In implantations.[13] Hence, we can assume that ^{119}Sb occupies the group-V lattice site and ^{73}Ga, the group-III site. In this way the use of radioisotopes allows a site-selective incorporation of the amphoteric Sn and Ge impurities.[13] The lattice location is to a large degree (>90%) unaffected by the recoil energies (E_R <2 eV for ^{119}Sb, $\bar{E}_R \sim 8$ eV for ^{73}Ga) and the possible charging effects (in the electron capture decay of ^{119}Sb) in the nuclear decays.[13]

B. Spectrometer

The instrument used for measuring the conversion electron spectra is a toroidal field, magnetic spectrometer of the Tretyakov type (2.65-m focal distance) with some modifications.[6] The source is surrounded by a cylindrical grid (diameter 11.6 cm) kept near ground potential. Spectra are recorded by stepping a positive high voltage V_s, applied to the source. Electrons leaving the source are decelerated in the electric field between source and grid and are then analyzed by the magnetic spectrometer, set for a constant energy $E_{\rm mag}$. The detector is a proportional counter (5 cm diameter and 10 cm length of the entrance window) with a resistive wire anode. Position is determined by charge division with 1–2-mm resolution. Arriving electrons are reaccelerated by placing the detector on a positive high voltage (14 kV) with respect to a grid of the same type as around the source. An electron detected at a position z relative to the center of the detector is assigned an energy

$$E = E_{\rm mag} + eV_s + z/D \ , \tag{4}$$

where D is the spectrometer dispersion. Spectra are constructed using a bin width equal to the step size of eV_s. The width of the resolution function is roughly given by $\Delta E = 0.01 E_{\rm mag}$ full width at half maximum (FWHM) and is independent of V_s. The spectrometer transmission has an approximate $1/E$ dependence, which can be corrected for. Since only the source voltage V_s is changed during a measurement, the background of a spectrum is energy independent (except for background originating directly from the source). Furthermore, the energy of the electrons arriving at the detector does not change when a spectrum is scanned, and thus the spectrum shape is not influenced by any energy-dependent detection efficiency, etc.

For the data reported here the spectrometer was set to $E_{\rm mag} = 200$ eV, corresponding to a resolution $\Delta E = 1.8$ eV (FWHM) and a dispersion $D = 10.6$ mm/eV. The resolution function is well understood and can therefore be taken accurately into account in the data analysis.[14] The calibration for $E_{\rm mag}$ is known to better than 1/2000, causing an error of less than 0.1 eV for the energies reported in this paper. Because of the large dispersion, the position of the source is also uncritical, and an estimated possible position error of 1 mm corresponds to an energy error of 0.1 eV. The source voltage V_s is measured with a relative error of about 20 ppm using a calibrated voltage divider and a precision voltmeter.

C. Data analysis

As an example, Fig. 3(a) shows the $L_{\rm II}$ and $L_{\rm III}$ lines of the 13 277-eV E2 transition to the ground state of ^{73}Ge, fed by the decay of ^{73}Ga (cf. Fig. 1). The $L_{\rm II}$ and $L_{\rm III}$ lines, originating from conversion in the L shell, have very small intrinsic widths, and these lines thus demonstrate the resolving power of the spectrometer. Each line is accompanied by a satellite line (labeled PL) due to the dominant energy-loss mechanism, which is plasmon excitation in the source material.

The experimentally observed conversion electron spectrum deviates in many respects from the ideal form given by Eq. (3). The lines acquire a Lorentzian width due to the lifetime of the final state (the hole in the shell from which the conversion electron was ejected). The conversion of an inner-shell electron may cause the excitation of an outer electron into a bound (shakeup) or continuum (shakeoff) state. This leads to satellites and tails at the low-energy side of the conversion lines. For conversion

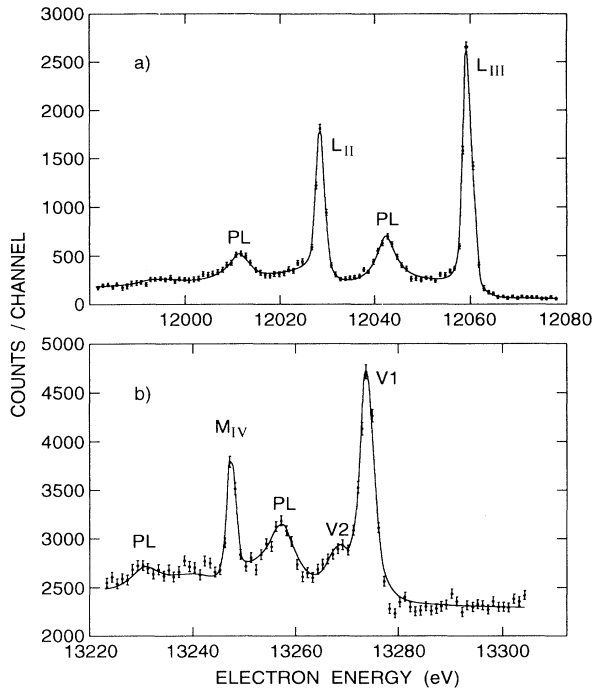

FIG. 3. (a) The L_{II} and L_{III} lines of the 13 277-eV $E2$ transition in ^{73}Ge fed by the decay of ^{73}Ga. A fit to the data, as described in the text, is included. (b) The $M_{IV,V}$ and valence part of the spectrum with corresponding analysis.

in the valence shell, this process is assumed to be negligible. While passing through the sample, the conversion electrons lose energy, mainly by plasmon excitation. This also leads to broad satellite lines. In half of all decays, the conversion electron is emitted into the sample, but may be backscattered into the solid angle of the spectrometer. This causes a flat and extended low-energy tail. The measurement is effectively a convolution of the spectrum as emitted from the source with the spectrometer resolution function. Finally, there is an energy-independent background from the detector.

In order to take these effects into account, the measured spectra are fitted to functions of the form

$$I_{\rm exp}(E)=R(E_{\rm mag})\oplus\left[B+\sum_n [L(E-E_n,\Gamma_n,A_n) +S_n^{\rm bs}+S_n^{\rm pl}+S_n^{\rm sh}]\right] . \quad (5)$$

Here, R is the known spectrometer resolution function [which has actually for simplicity been replaced by a Gaussian with a width (FWHM) of 1.8 eV], and $\oplus$ denotes convolution. The background B is assumed to be energy independent. A conversion line is represented by a Lorentzian,

$$L(E-E_n,\Gamma,A)=A(\Gamma/\pi)/[(E-E_n)^2+\Gamma^2] , \quad (6)$$

with amplitude A, central energy E_n, and width Γ.

The shakeup and shakeoff $S_n^{\rm sh}$ usually appears as an exponential tail and was represented by terms of the form

$$S_n^{\rm sh}(E-E_n,\alpha,\beta,A) = A\ \mathrm{erfc}[\beta(E-E_n)]\exp[\alpha(E-E_n)] , \quad (7)$$

with an amplitude A and a decay constant α. A cutoff with the complementary error function with scale parameter β was found to be a reasonable choice.

The backscattering tail was also assumed to be of the form of Eq. (7) with α close to zero. Its intensity ($I_{\rm bs}$) was measured in an independent experiment[6] for C, Si, and Cu substrates and an initial energy $E_i=19.4$ keV. Roughly, $I_{\rm bs}$ is proportional to the average Z of the substrate and inversely proportional to E_i. For the present samples we estimate $I_{\rm bs}$ to be 0.05–0.1/keV, which is small considering the narrow energy range of the valence electrons.

The form of the energy-loss function $S_n^{\rm pl}$ was taken to be of Drude type:[15]

$$S_n^{\rm pl}(\Delta,A,E_p,W)=\frac{-A\Delta}{(\Delta^2-E_p^2)^2+(W\Delta)^2} , \quad \Delta=E-E_n\le 0 \quad (8)$$

for a single interaction, with an amplitude A, a plasmon energy of E_p, and a width parameter W. The energy-loss distribution for electrons suffering multiple (N) interactions is given by N convolutions of Eq. (8) with itself. In practice, the source thickness was chosen so that the two-plasmon excitation is always below the 10% level and higher-order excitations are negligible.

Figure 3(a) shows a fit to the L_{II} and L_{III} lines for the 13277-eV transition in ^{73}Ge, and the essential parameters are listed in Table I. The relative fractions f_i are the relative areas of the spectral components with the sum normalized to 1. The shake and backscattering fractions have been summed since in most cases they cannot be independently identified, as they are of the same functional form. The plasmon fraction is about 65% of the Lorentzian intensity (the no-loss fraction). For these inner lines the shake fractions are very large. Table I also contains results obtained for other closed-shell measurements, and the important observations are the following.

(1) The plasmon energy-loss to no-loss ratio does not differ significantly from shell to shell. This is to be expected since the mean free path for inelastic interactions is approximately proportional to $1/E$ and the energies of the measured lines are of similar magnitude.

(2) With increasing Z of the target, the same ratio decreases. This is due to a delicate balance between the influence of the depth distribution of the implanted impurities and that of the plasmon loss probability.

(3) The shake fractions are decreasing dramatically when going from the inner towards the outer shells, demonstrating that this phenomenon originates in the internal conversion process itself.

Figure 3(b) shows a ^{73}Ge $M_{IV,V}$ and valence spectrum from the same transition and the corresponding analysis. As can be seen from the figure and from Table I, the spectrum is well fitted without invoking any shake or

TABLE I. Results from a least-squares-fit analysis of conversion lines from ^{73}Ge and ^{119}Sn. The relative Lorentzian f_L, plasmon energy loss f_{pl}, and shake and backscattering fractions f_{bs+sh} are given. The errors on f_{bs+sh} for the valence lines are estimates of possible hidden fractions.

Isotope	Host	Line	f_L	f_{pl}	f_{bs+sh}	f_L/f_{pl}
^{73}Ge	Si	Valence	0.60(2)	0.40[a]	0.00(10)	1.5[a]
		M_{IV}	0.46(2)	0.31[a]	0.23(10)	1.5[a]
		$M_{II}+M_{III}$	0.34(1)	0.23(2)	0.43(4)	1.5(1)
		$L_{II}+L_{III}$	0.25(1)	0.15(1)	0.60(6)	1.7(1)
	GaAs	$L_{II}+L_{III}$	0.27(1)	0.13(1)	0.60(5)	2.0(1)
^{119}Sn	Si	Valence	0.78(5)	0.22[a]	0.00(15)	3.6[a]
		N_I	0.36(1)	0.10(1)	0.54(2)	3.6(4)

[a]A fixed parameter in the analysis.

backscattering components, although the presence of a small contribution cannot—due to the limited energy range measured—be excluded. In the analysis the plasmon loss to no-loss ratio has been fixed to the value obtained from the M shells, and very good agreement is obtained.

The analysis of the ^{119}Sn spectra is less complicated, since the Xe ions have a shorter range and the conversion electron energies are higher, making the energy-loss problems less severe. Table I contains typical ^{119}Sn results as well.

In the further processing of the valence spectra, the fitted background, backscattering fractions (hardly ever used for the valence spectra), and plasmon fraction are subtracted from the data. What remains is a spectrum of the form of Eq. (3); however, it is convoluted with the experimental resolution function. The analysis procedure induces little or no distortion in the last 10 eV below the Fermi level, whereas deeper features may suffer some distortion from the subtraction of the plasmon fraction. The background subtraction can in principle influence the integral of the valence spectrum, but not its shape.

D. Determination of the Fermi level

To determine the Fermi-level energies as defined by Eq. (2), all conversion lines were measured with the corresponding elemental samples, i.e., for ^{119}Sn in β tin and for ^{73}Ge in Ge, where by definition there is no chemical shift. In the case of ^{73}Ge also, results of measurements with a Si host were used, since the chemical shift between these two hosts is negligible. For these cases accurate binding energies are available.[1,16] The measured centroid energies and binding energies are listed in Table II for ^{119}Sn and in Table III for ^{73}Ge. As is seen, the sum of the two energies is constant within errors. By taking an average, we obtain the Fermi energies also given in the tables.

The Fermi energies thus determined correspond to the highest possible conversion electron energy. By inspection of the spectra recorded so far, the cutoff energies listed in the tables have been extracted. These are in perfect agreement with the Fermi energies determined from measurements on the closed shells, and this fact constitutes an independent check of the Fermi-energy determination. The Fermi energies determined have errors of 0.2 and 0.6 eV, respectively, for ^{119}Sn and ^{73}Ge, and are reproducible within 0.2 eV.

For the semiconductors studied here, the annealing procedures used were sufficient to remove most of the lattice damage from the implantation process, but insufficient to cure the pinning of the Fermi level in the middle of the band gap. When comparing to the theoretical calculations, we therefore use this energy reference. This procedure may introduce in the worst case an error

TABLE II. ^{119}Sn conversion line energies E_{CE}, atomic binding energies E_B, and the deduced Fermi-level energies $E_{CE}(F)$. Also indicated is the cutoff energy, which is the maximum conversion electron energy observed.

Shell	E_{CE} (eV)	E_B (eV)	$E_{CE}(F)$ (eV)
L_{II}	19 718.0(3)	4156.1(3)	23 874.1(4)
L_{III}	19 945.3(3)	3928.8(3)	23 874.1(4)
M_I	22 989.0(5)	885.3(9)	23 874.3(1.0)
M_{II}	23 117.3(3)	756.6(3)	23 873.9(4)
M_{III}	23 159.4(5)	714.7(3)	23 874.1(6)
N_I	23 736.5(3)	137.2(7)	23 873.7(8)
Cutoff	23 874.0(5)	≡0	23 874.0(5)
$\overline{E_{CE}(F)}$			23 874.0(2)

TABLE III. ^{73}Ge conversion line energies E_{CE}, atomic binding energies E_B, and the deduced Fermi-level energies $E_{CE}(F)$. Also indicated is the cutoff energy, which is the maximum conversion electron energy observed.

Shell	E_{CE} (eV)	E_B (eV)	$E_{CE}(F)$ (eV)
K	2174.0(3)	11 103.1(7)	13 277.1(8)
L_{II}	12 028.9(2)	1248.1(7)	13 277.0(7)
L_{III}	12 060.1(2)	1217.0(7)	13 277.0(7)
M_{II}	13 151.1(2)	124.9(2)	13 276.0(3)
M_{III}	13 155.4(2)	120.8(2)	13 276.2(3)
M_{IV}	13 247.6(1)	29.9(1)	13 277.5(2)
Cutoff	13 277.0(3)	≡0	13 277.0(3)
$\overline{E_{CE}(F)}$			13 276.8(6)

in the energy definition of $E_G/2$, where E_G is the energy gap of the material in question.

IV. DETAILS OF COMPUTATIONS

The present calculations of the electronic structure of isolated impurity atoms in a crystalline environment are done with the self-consistent linear-muffin-tin-orbital (LMTO) Green's-function method.[7,17] Several *ab initio* impurity Green's-function methods have been developed and applied to realistic solid-state systems (see, e.g., Refs. 18, 19, 20, and 7). The LMTO Green's-function method has been successfully applied to impurities in semiconductors,[21,17,22] insulators,[23] and metals.[24] Similar to the majority of other Green's-function methods, the LMTO method invokes the local-density approximation[25,8] (LDA), i.e., each electron moves in an effective potential, which includes exchange and correlation effects through a simple local term. The valence electronic structure of the impurity atom is obtained from the solid Green's function G, which is found by solving the Dyson equation

$$G = G^0 + G^0 \Delta V G \ , \tag{9}$$

where G^0 is the Green's function of the pure crystal host and ΔV the perturbation due to the impurity. In the LMTO method the host Green's function is calculated from the band structure of the pure crystal in the orthogonal approximation[7] and with the atomic spheres approximation (ASA), i.e., the crystal volume is approximated by slightly overlapping atom centered spheres, inside which the potential is taken spherically symmetric. Due to the open ZnS structure of the III-V compounds, additional spheres are introduced centered on the tetrahedral interstitial sites.[26] By a simple scaling, Eq. (9) may be cast into a particularly simple form, where the perturbation enters only through the logarithmic derivatives of the impurity potential on the sphere boundary. The resulting matrix equation attains the size of the number of atomic spheres in the perturbed region times the number of basis functions inside each sphere. Since screening is rather effective in solids, it suffices to include the impurity atom and the shell of nearest-neighbor spheres (four atomic and four empty in the case of a substitutional impurity in III-V semiconductors) as the perturbed region. The LMTO method, furthermore, employs numerical basis functions given by solutions of the scalar-relativistic Dirac equation at a representative energy, which means that only one set of partial waves of s, p, d, and possibly f character is needed inside each sphere to obtain an accurate description of the electronic structure. Hence, the LMTO Green's-function method is numerically extremely effective. A natural output is the perturbed density of valence states projected onto the impurity sphere and decomposed according to its angular momentum character, which is exactly the crucial quantity in Eq. (3). Specifically, the local density of states for each angular momentum channel is given by

$$N_l(E) = \frac{1}{\pi} \sum_m \mathrm{Im} G_{lm,lm}(E) \ , \tag{10}$$

where $G_{lm,l'm'}(E)$ are the matrix elements of the perturbed Green's function between (orthogonal) muffin-tin orbitals centered on the impurity site. Some ambiguity persists as to the size of the sphere around the impurity atom onto which the density of states is projected. In this work we consistently choose all spheres to have the same size determined by the experimental host lattice constant, whereby the geometrical approximations of the ASA are minimized.

In the calculations presented here we have used the

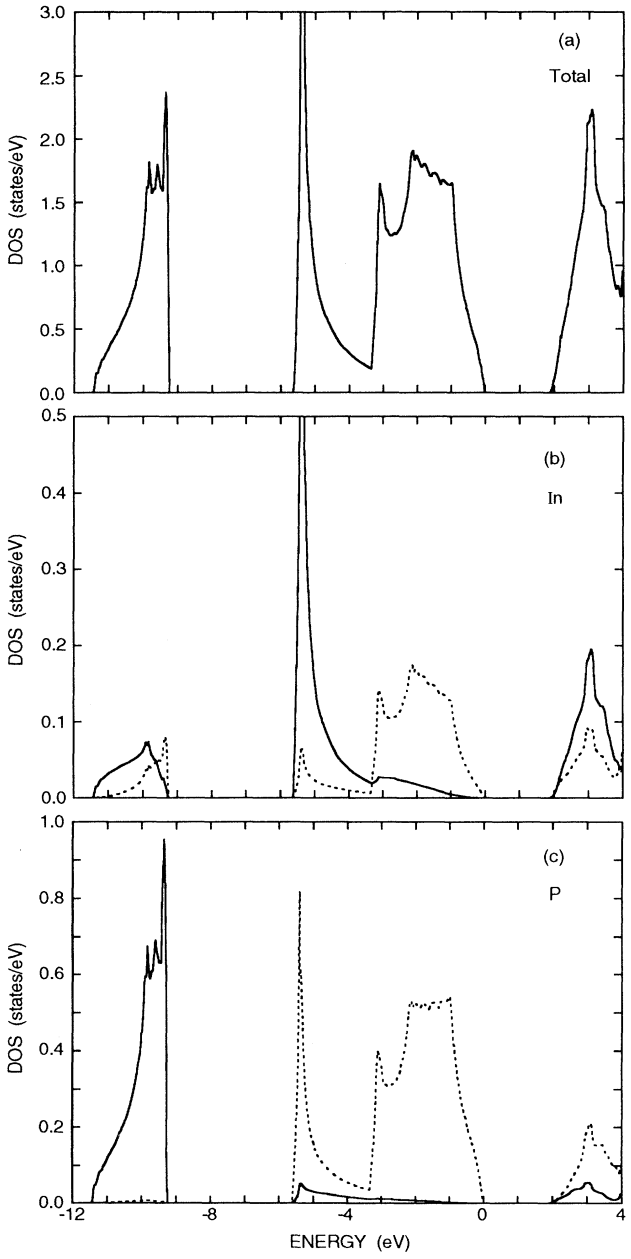

FIG. 4. (a) Total, (b) In, and (c) P projected density of states of InP. Units are electrons per eV and spin and unit cell (a) or atom [(b) and (c)]. The solid line is the s component, the dashed line the p component.

"standard" basis set for the diamond structure,[26] which includes partial waves of *s*, *p*, and *d* character on each atomic and interstitial site to give a total of 36 LMTO orbitals per unit cell. The unperturbed Green's function is calculated with the tetrahedron method[7] using 95 **k** points in the irreducible wedge of the Brillouin zone and two energy panels to cover all of the 36 LMTO bands. The drawback of the LDA of producing band gaps in semiconductors that are too small is remedied by applying the scissors operator, i.e., the conduction bands are rigidly shifted upwards to reproduce the experimental minimum gap. The impurities considered are all ideal substitutional ones, i.e., no relaxation of the neighboring atoms is allowed for.

In Fig. 4 we show the InP density of states as computed with this approach. Figure 4(a) gives the total crystalline density of states, while Figs. 4(b) and 4(c) depict the projections onto the In and P atomic spheres, respectively. The lowest valence band is predominantly a P *s* like one and is separated by a 3.7-eV gap to the wide second-lowest valence band, which is of mixed In *s* and P *p* character. The two uppermost valence bands are less dispersive and are dominated by bands of P *p* character. In Table IV we compare the value of the valence-band edges of the hosts considered in this work to the results of angular resolved photoemission experiments. The agreement is rather good, with all deviations within ~0.4 eV, thus demonstrating the accuracy of the LDA in determining the valence-band structure of III-V semiconductors. There is a clear trend, though, with slightly smaller theoretical dispersion than observed experimentally. In contrast to this rather accurate description of the valence bands, the fundamental gaps are not so well calculated in the LDA. The best LDA calculation of the GaAs band gap yields only 0.25 eV,[30] whereas the experimental value is 1.52 eV. The present calculation gives a gap of 1.41 eV, which by chance is close to the experimental value. It is well established that when corrections for the ASA and the partial-wave cutoff (the "combined correction"[31]) are invoked in the computation, the fundamental gap tends to diminish.[26,30] These corrections are not applied in the host calculations used here, since the consequential application of the same corrections in the impurity calculation is rather cumbersome, albeit in principle possible. Thus, the scissors-operator shift is taken to be 0.11 eV in GaAs. Similarly, the shifts in GaP and InP are 0.84 and 0.45 eV, respectively, to reproduce the experimental (zero-temperature) minimum gaps of 2.32 and 1.42 eV.

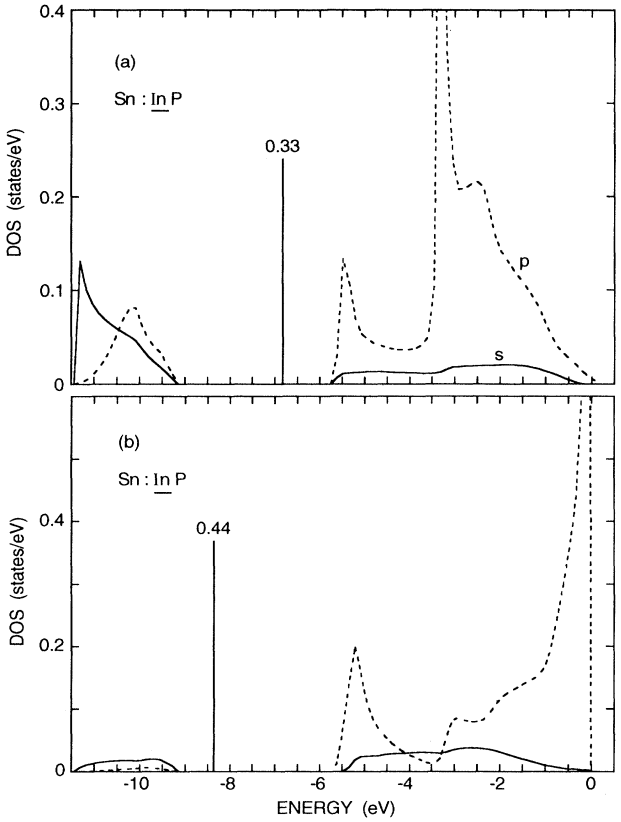

FIG. 5. Projected density of states of a substitutional Sn atom in InP: (a) on an In site and (b) on a P site. Units are as in Fig. 4. The vertical bar marks the bound *s*-like state in the valence-band gap and the corresponding spectral weight is indicated.

In Fig. 5 is depicted the projected density of states for

TABLE IV. Valence-band edges of the GaAs, InP, and GaP hosts in eV relative to the Γ_{15} valence-band maximum. W is the width of the valence-band gap in eV.

	GaAs		InP		GaP	
	Theor.	Expt.[a]	Theor.	Expt.[b]	Theor.	Expt.[c]
Γ_1	−12.73	−13.1	−11.44	−11.4	−12.45	−12.5
X_1	−10.36	−10.75	−9.29	−9.6	−9.60	−9.9
X_3	−6.74	−6.70	−5.64	−5.9	−6.68	−6.8
X_5	−2.56	−2.80	−2.22	−2.45	−2.59	−3.0
L_1	−11.07	−11.24	−9.91	−10.0	−10.48	−10.7
L_2	−6.59	−6.70	−5.65		−6.60	−6.7
L_3	−1.10	−1.30	−0.93	−1.0	−1.08	−1.0
W	3.62	4.05	3.64	3.7	2.92	3.1

[a]Reference 27.
[b]Reference 28.
[c]Reference 29.

TABLE V. Calculated position E_b of the bound s-like state of substitutional Sn and Ge in III-V hosts. For Sn_V the experimental positions from Sec. V are given. Units are eV and relative to the Fermi level, which is assumed to coincide with the middle of the band gap. For comparison with Table IV and Figs. 4 and 5, the zero of energy is shifted upwards by 0.65, 0.70, and 1.10 eV for InP, GaAs, and GaP, respectively. Also listed is the calculated occupation n of the bound state on the impurity sphere (including a factor of 2 for spin).

		^{73}Ge		^{119}Sn		
Host	Site	n	E_b	n	E_b	E_b (expt.)
GaAs	III	0.74	−8.00	0.60	−8.23	
	V	0.93	−8.45	0.70	−8.95	−7.72±0.12±0.21
GaP	III	0.55	−7.81	0.49	−8.48	
	V	0.82	−8.37	0.63	−9.37	−8.84±0.11±0.21
InP	III	0.76	−7.28	0.66	−7.44	
	V	1.07	−8.06	0.88	−8.54	−8.21±0.11±0.21

a Sn atom on either the In or the P site in InP. In both cases a bound state of s-type symmetry is formed in the valence-band gap between the lowest and the three upper valence bands. When Sn replaces a P atom, the perturbing potential is repulsive and of sufficient strength to locally force the s weight above the lowest P s-derived valence band, thereby forming the bound state. On the other hand, when Sn replaces an In atom, the perturbing ΔV is attractive and sufficiently strong to bind a state below the upper three valence bands. In both cases most of the local s-like character, previously distributed over the entire energy-band region of the pure host, is removed and energetically pinned at the position of the bound state. The same phenomenon takes place for a substitutional Ge atom, and in the GaAs and GaP hosts as well. Table V lists the details of this bound state. Note that this table gives energies relative to the middle of the room-temperature gap to ease comparison between theory and experiment. This means that the zero of energy is taken 0.65, 0.70, and 1.10 eV above the valence-band maximum for InP, GaAs, and GaP, respectively. For Sn replacing a V atom, the calculated position of the bound state is 1.41, 0.75, and 0.23 eV above the lowest valence band in GaAs, InP, and GaP, respectively. For a Ge impurity atom, these energy levels are calculated as 1.91, 1.23, and 1.23 eV above the lowest valence band. When the impurity replaces a group-III atom, the bound state is pulled 1.49, 1.79, and 1.80 eV below the upper three valence bands, in the case of a Sn impurity, and 1.26, 1.63, and 1.13 eV in the case of a Ge impurity, for the same host crystal sequence, GaAs, InP, and GaP. In all cases the Ge level lies above the corresponding Sn level.

V. RESULTS AND DISCUSSION

In Figs. 6–8 are shown the experimental valence-electron spectra, with background and energy-loss components subtracted, as described in Sec. III C, for substitutional Sn atoms on the V site in GaAs, GaP, and InP

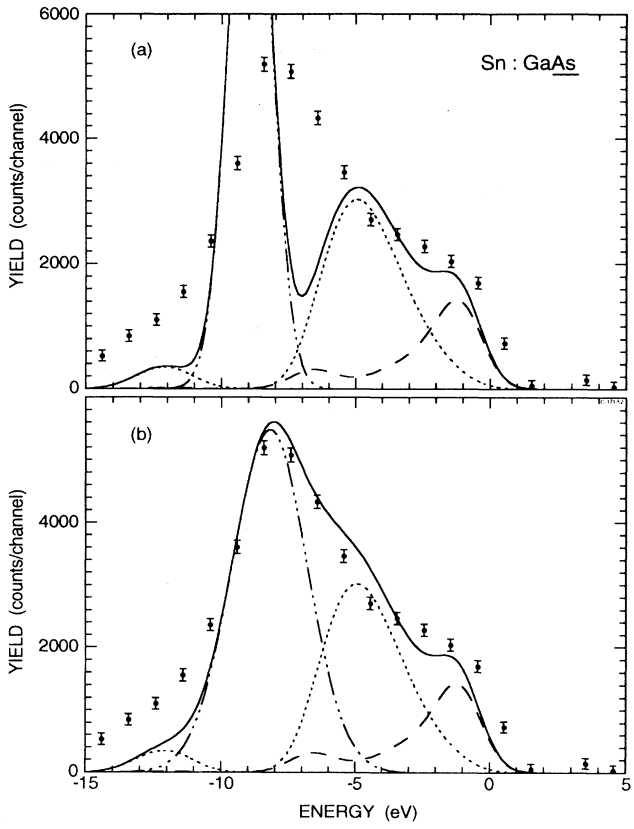

FIG. 6. Experimental (•) and theoretical (solid line) conversion electron spectrum for substitutional Sn atom on an As site in GaAs. Shown also are the components of the calculated spectrum due to the s-like bound state (dash-dotted), and the Sn s character (dotted) and p character (dashed) in the valence bands. In (a) the calculated impurity density of states is broadened by a 1.8-eV Gaussian, while in (b) the bound-state component is broadened by a 3.3-eV Gaussian and its position is shifted by 0.75 eV towards higher energies.

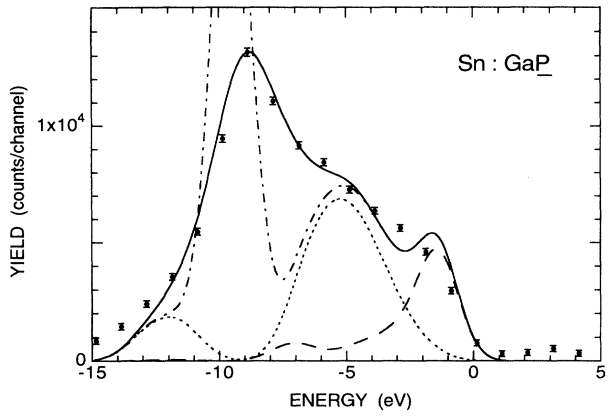

FIG. 7. Experimental (•) and theoretical conversion electron spectrum for a substitutional Sn atom on a P site in GaP. The dash-dotted curve shows the theoretical spectrum broadened by a 1.8-eV Gaussian. In the solid curve the bound-state component has been shifted upwards by 0.6 eV and broadened by a 3.3-eV Gaussian. The dotted and dashed curves give the s and p components of the continuum states.

together with the calculated spectra. Figure 10 show results for Ge on the III site in GaAs and InP.

The theoretical spectra are obtained from the calculated impurity projected density of states, of which Fig. 5 shows an example. The angular momentum components are multiplied by the conversion coefficients [$P(M,n,l)$ in Eq. (3)] and convoluted with a Gaussian to simulate the effect of the experimental resolution function. For the Sn $M1$ transition we use the ratio of conversion coefficients

$$P_{\mathrm{Sn}}(M1,5,s):P_{\mathrm{Sn}}(M1,5,p)=90:10$$

(Ref. 32), while for the $E2$ transition of Ge we take this ratio as

$$P_{\mathrm{Ge}}(E2,4,s):P_{\mathrm{Ge}}(E,2,4,p)=25:75\ .$$

Some uncertainty persists on these ratios, especially for the Ge transition. For all the cases studied we used the spectrometer resolution (1.8 eV FWHM) as the width of the broadening Gaussian. However, for the case of ^{119}Sn, this gave a rather poor agreement with experiment and therefore we also assumed a significantly larger broadening for the bound state. In that way the detailed shape of the measured spectra was reproduced much better. In addition, the position of the bound state in the valence-band gap seems consistently to be calculated slightly too low in comparison with experiment. This implicates that some broadening mechanism other than that due to the spectrometer (e.g., lifetime effects or residual damage in the vicinity of the impurity atom) influences the bound-state data. Most likely, it is the higher doses in the case of the Sn implantations, which cause higher levels of residual damage after annealing. This conclusion is also corroborated by the fact that for Sn in InP we have found no visible effect on the measured spectra whether we set the spectrometer resolution to 0.9 or 1.8 eV. Another parameter needed to fix the relative position of theoretical and experimental data is the position of the Fermi level. We expect our samples to be essentially intrinsic, so for the theoretical figures we align the Fermi level with the middle of the band gap.

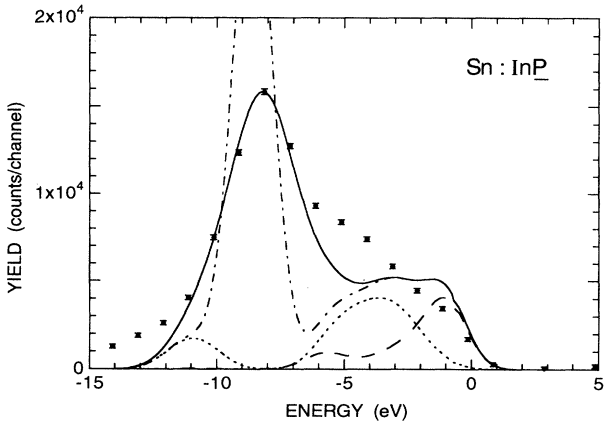

FIG. 8. Experimental (•) and theoretical conversion electron spectrum for a substitutional Sn atom on a P site in InP. The dash-dotted curve shows the theoretical spectrum broadened by a 1.8-eV Gaussian. In the solid curve the bound-state component has been shifted upwards by 0.3 eV and broadened by a 3.3-eV Gaussian. The dotted and dashed curves give the s and p components of the continuum states.

A. Results for ^{119}Sn

The spectra of Sn substituting a group-V atom in the III-V semiconductors (Figs. 6–8) are all very similar. There is a major peak at around E_F-8 eV, and a broad shoulder on the high-energy side of this peak extending all the way to the Fermi level. This form of the spectra is also qualitatively found in the theoretical curves, although with some minor quantitative discrepancies.

Figure 6 shows the comparison of experiment and theory for Sn:GaAs. In Fig. 6(a) is shown the calculated spectrum after broadening all features with a 1.8-eV Gaussian, while Fig. 6(b) shows the calculated spectrum after broadening the bound-state component by a 3.3-eV Gaussian and shifting its position upwards by 0.75 eV, while the rest of the calculated impurity density of states is treated as in Fig. 6(a). In both cases the experimental conversion electron spectrum is superposed with appropriate error bars. In addition, the decomposition of the theoretical curves into components stemming from the bound state and from the s and p parts of the impurity density of states is shown. Figure 6(a) demonstrates the qualitative agreement between theory and experiment, but it appears that a 1.8-eV broadening of the bound-state component of the theoretical spectrum leads to a much narrower peak than observed. From Fig. 6(b) it is seen that extra broadening and shifting of the bound-state component lead to an excellent accordance between theory and experiment in the entire 10-eV range of the GaAs valence band. From the decomposition of the theoretical curve in Fig. 6(b), it is seen that the primary peak is due to the bound state, while the broad

shoulder is caused by a mixture of the Sn s character in the upper valence bands and the Sn p character of the highest valence-band region. The number of Sn p electrons in the valence bands is significant [cf. Fig. 5(b)], but due to the small conversion probability for p electrons, they contribute less than the s electrons to the total spectrum. The p-electron component is, however, important for the shape of the shoulder, in particular for the steep increase just below the Fermi level. Table V gives the experimental and theoretical bound-state energies for the Sn on a V site. The results agree within ~ 1 eV. The experimental values were obtained by making a decomposition of the valence-band spectra in terms of two or three Lorentzians [cf. Fig. 3(b)]. From Fig. 6(b) it is seen that the maximum of the spectrum is shifted away from the position of the bound state due to the overlap with the continuum component. The fact that the calculated and measured spectra do not fall on top of each other at the Fermi level may be an indication that the actual Fermi-level position is not in the band-gap center but rather in the upper part of the GaAs band gap as for n-type material.

For Sn in GaP (Fig. 7) the shoulder and primary peak are less separated experimentally than was found in GaAs, while the calculated curve is very similar to that of Fig. 6. The rise of the shoulder at the Fermi level is well reproduced in the calculations, but the primary peak is found too narrow and too low. So, similar to GaAs, by broadening the bound-state feature somewhat and moving the bound state 0.6 eV above the actually calculated position, the experimental data are very well reproduced. So, again, the bound state seems to be calculated too low compared with experiment. This may be an intrinsic failure of the LDA, although it opposes the effect discussed in connection with Table IV of finding too little dispersion (i.e., energies that are too *high*) of the host electronic states in the LDA. Another likely cause for the too large calculated binding energy of the bound state is the neglect of atomic relaxations around the impurity atom. The small extra feature at -1.7 eV in the calculated spectra (which originates from Sn p electrons) is not resolved experimentally, but we note that an only slightly higher s:p conversion ratio will cause it to disappear from the theoretical curve.

For Sn in InP (Fig. 8) we find essentially similar results. The primary peak is more pronounced in the experimental spectra than for the GaAs and GaP cases. Theoretically, we also find a larger weight of the bound state on the Sn atomic sphere, namely, 0.88 of the two electrons, as opposed to 0.70 and 0.63 for GaAs and GaP, respectively. Again, we have found it necessary to shift the bound state slightly upwards (by 0.3 eV) and to broaden it. The shoulder above the primary peak is less well reproduced, but we note that the agreement would be improved had we assumed a somewhat larger broadening for the continuum part of the spectrum.

It would be interesting to study a Sn atom on a III site, since the theory predicts a distinctly different conversion electron spectrum. For a Sn atom on an In site in InP, we would from Fig. 5(a) expect a three-peak structure, since the appreciable Sn s character in the lowest valence band would yield a significant component. The bound state has less weight than for a Sn atom on the P site [Fig. 5(b)], i.e., the primary peak would be less pronounced, and for the low binding-energy shoulder, a less distinct rise at the Fermi level is predicted, since the Sn p character in Fig. 5(a) does not trail the top valence-band edge. Figure 9 shows the predicted conversion electron spectrum for Sn on an In site in InP. Experimentally, the study of this system would be feasible using the radioisotope ^{119}In (see Fig. 1), which is available with good yields from ISOLDE. The short half-life (2.9 min) would, however, require the electron spectrometer to be connected on line to the mass separator delivering the radioactive beam.

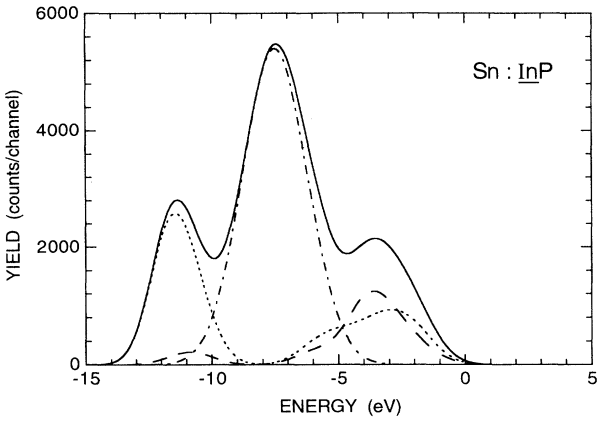

FIG. 9. Theoretical (solid line) conversion electron spectrum for a substitutional Sn atom on an In site in InP. Shown also are the components of the calculated spectrum due to the bound state (dash-dotted) and the Sn s character (dotted) and p character (dashed) in the valence bands.

B. Results for ^{73}Ge

The conversion electron spectra of Ge in Figs. 10(a) and 10(b) are distinctly different from the Sn spectra, since the Ge transition primarily probes the p character of the Ge projected density of states. The experimental spectra are dominated by a large peak around 4 eV below the Fermi level with a small shoulder towards lower energies. In the theoretical spectra there is also a dominating peak stemming from the Ge p character in the upper valence bands, while the s-like bound state and the s and p character of the lowest valence band give rise to two small humps at large binding energies. Experimentally, the two-hump structure in the shoulder is not resolved, but, as previously stated, some uncertainty is connected with the measured spectra at energies below $E_F - 10$ eV.

For Ge in GaAs, in Fig. 10(a), the accordance between theory and experiment is good. The primary peak positions do not coincide precisely, but would do so provided the experimental Fermi level is shifted by ~ 1 eV. This would also place the -8.5-eV hump (stemming from the bound state) on top of the shoulder observed. We note that the experimental statistics are poorer than for the Sn spectra.

For Ge in InP [Fig. 10(b)], the measured primary peak is somewhat narrower than in GaAs [Fig. 10(a)]. In addition, it is more asymmetric with a steep descent on the low-energy side. This is in accordance with the shape of the unbroadened theoretical impurity p density of states in Fig. 5(a). As for GaAs, the size of the shoulder is underestimated in theory and the shape ill reproduced.

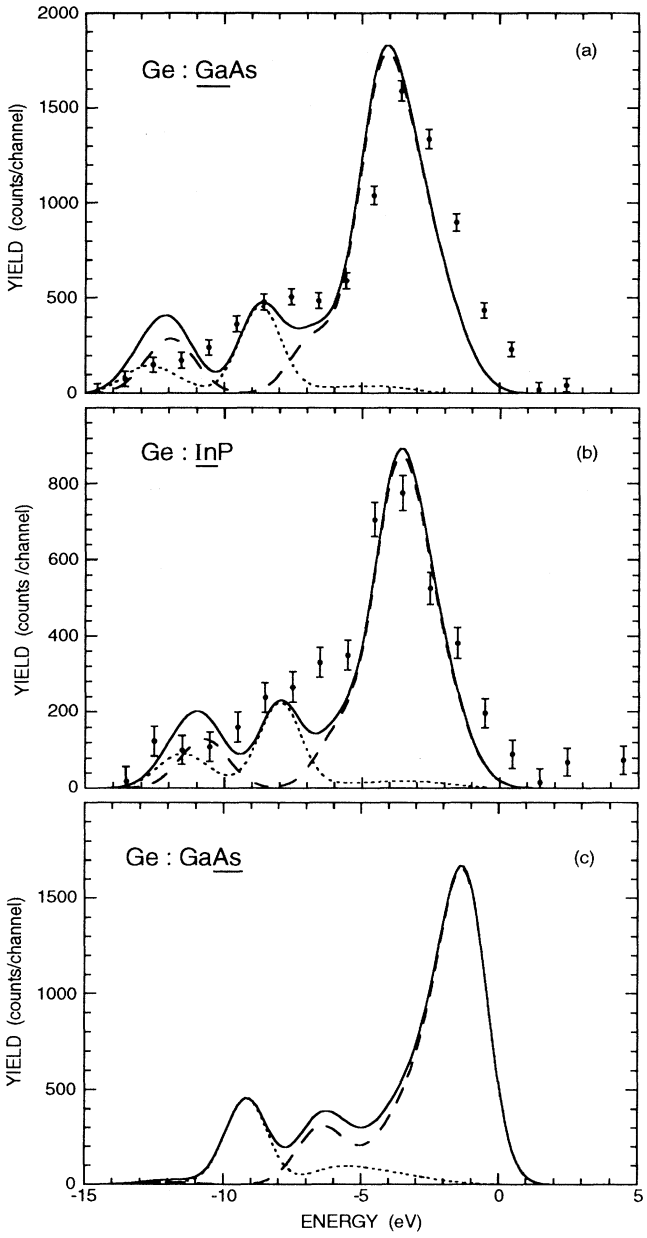

FIG. 10. (a) Experimental (●) and theoretical (solid line) conversion electron spectrum for a substitutional Ge atom on a Ga site in GaAs. Shown also are the components of the calculated spectrum due to the Ge s character, including the bound state (dotted) and p character (dashed) in the valence bands. (b) Same for a substitutional Ge atom on an In site in InP. (c) Theoretical (solid line) conversion electron spectrum for a substitutional Ge atom on an As site in GaAs. Shown also are the components of the calculated spectrum due to the Ge s character, including the bound state (dotted) and p character (dashed) in the valence bands.

Measurements of Ge conversion electron spectra from Ge atoms residing on a V site would be rather similar to those of Figs. 10(a) and 10(b). There would still be a dominating p-derived peak in the upper valence region, now with a steep descent towards the Fermi level, and a two-hump structure towards larger binding energies. The total width of the spectra would be smaller, since essentially no Ge weight resides in the lowest valence band. On the other hand, the integrals of the spectra would be substantially different, especially for InP. Figure 10(c) shows a theoretical spectrum for Ge on an As site in GaAs. Experimentally, this system may be studied in the future, since strong beams of long-lived ^{73}As have become available at ISOLDE. Using ^{73}As would lead to ^{73}Ge being incorporated on the V site.

VI. CONCLUSIONS

In this paper it has been shown that high-resolution conversion electron spectroscopy can be used to extract useful information about the electronic structure of dilute probe atoms in solids. The method delivers spectroscopic information on the energy dispersion of the local density of states around the impurity atom. It has been demonstrated that sufficient signal can be obtained for resolutions down to 1.8 eV. Data for substitutional Sn and Ge impurity atoms in several III-V compounds have been obtained using a site-selective ion-implantation technique. The general usefulness of conversion electron spectroscopy is restricted by the need to prepare thin and strong radioactive sources containing the element under study. On the other hand, some forty elements, which possess isotopes with suitable transitions, can be identified. This makes conversion electron spectroscopy more general in practical use than other nuclear methods used in solid-state experiments.

The experimental results have been compared to theoretical calculations, which were performed with the first-principles linear-muffin-tin-orbitals Green's-function method. The calculations predict the local density of states around a substitutional Sn or Ge atom on a III and on a V site to be dominated by an s-like bound state in the valence-band gap some 8 eV below the Fermi level. The existence and the binding energies of these states have been confirmed by the experimental results. Binding-energy discrepancies are within the systematic uncertainties of the data. They can either be due to simplifications in the theoretical calculations, e.g., the treatment of exchange and correlation effects in the local-density approximation or the neglect of relaxation around the impurities, or to residual damage effecting the experimental results. We plan to make progress in both directions in the future.

ACKNOWLEDGMENT

This work was supported by the Danish Accelerator Research Council.

[1]*Topics in Applied Physics,* edited by M. Cardona and L. Ley (Springer, Berlin, 1978), Vols. 26–27.
[2]See, e.g., *Proceedings of the Fifteenth International Conference on Defects in Semiconductors,* edited by G. Ferenczi (Trans Tech, Aedermannsdorf, Switzerland, 1989).
[3]See, e.g., Nucl. Instrum. Methods B **63**, 179 (1992).
[4]F. Rosel, H. Fries, K. Adler, and H. C. Pauli, At. Data Nucl. Data Tables, **21**, 91 (1978), and references cited therein.
[5]T. A. Carlson, P. Erman, K. Fransson, Nucl. Phys. A **111**, 371 (1968).
[6]M. Fritschi, E. Holzschuh, W. Kundig, J. W. Petersen, R. E. Pixley, and H. Stussi, Phys. Lett. B **173**, 485 (1986).
[7]O. Gunnarsson, O. Jepsen, and O. K. Andersen, Phys. Rev. B **27**, 7144 (1983).
[8]R. O. Jones and O. Gunnarsson, Rev. Mod. Phys. **61**, 681 (1989).
[9]N. E. Christensen, Phys. Rev. B **30**, 5753 (1984).
[10]J. W. Petersen, G. Weyer, E. Holzschuh, and W. Kündig, Phys. Lett. A **146**, 226 (1990).
[11]J. W. Petersen, G. Weyer, A. Svane, E. Holzschuh, and W. Kündig, Nucl. Instrum. Methods B **63**, 179 (1992).
[12]H. L. Ravn, Phys. Rep. **54**, 201 (1979).
[13]G. Weyer, J. W. Petersen, S. Damgaard, and H. L. Nielsen, Phys. Rev. Lett. **44**, 155 (1980).
[14]M. Fritschi, E. Holzschuh, W. Kündig, and H. Stüssi, Nucl. Phys. (Proc. Suppl.) B **19**, 205 (1991).
[15]H. Raether, in *Excitations of Plasmons and Interband Transitions by Electrons,* edited by G. Hohler, Springer Tracts in Modern Physics Vol. 88 (Springer, Berlin, 1980), p. 84.
[16]K. D. Sevier, At. Data Nucl. Data Tables **24**, 323 (1979).
[17]M. J. Puska, O. Jepsen, O. Gunnarsson, and R. M. Nieminen, Phys. Rev. B **34**, 2695 (1986).
[18]G. A. Baraff and M. Schlüter, Phys. Rev. B **19**, 4965 (1979).
[19]R. Podloucky, R. Zeller, and P. H. Dederichs, Phys. Rev. B **22**, 5777 (1980).
[20]A. Zunger, Solid State Phys. **39**, 275 (1986).
[21]F. Beeler, M. Scheffler, O. Jepsen, and O. Gunnarsson, Phys. Rev. Lett. **54**, 2525 (1985); F. Beeler, O. K. Andersen, and M. Scheffler, *ibid.* **55**, 1498 (1985).
[22]A. Svane, J. Phys. C **21**, 5369 (1988).
[23]G. Timmer and G. Borstel, Phys. Rev. B **43**, 5098 (1991).
[24]A. Svane, Phys. Rev. Lett. **60**, 2693 (1988).
[25]P. Hohenberg and W. Kohn, Phys. Rev. **136**, B864 (1964); W. Kohn and L. J. Sham, *ibid.* **140**, A1133 (1965).
[26]D. Glötzel, B. Segall, and O. K. Andersen, Solid State Commun. **36**, 403 (1980).
[27]T. C. Chiang, J. A. Knapp, M. Aono, and D. E. Eastman, Phys. Rev. B **21**, 3531 (1980).
[28]*Numerical Data and Functional Relationships in Science and Technology,* edited by O. Madelung (Springer, Berlin, 1989), Vol. 23.
[29]F. Solal, G. Jezequel, F. Houzay, A. Barski, and R. Pinchaux, Solid State Commun. **52**, 37 (1984).
[30]G. B. Bachelet and N. E. Christensen, Phys. Rev. B **31**, 879 (1985).
[31]O. K. Andersen, Phys. Rev. B **12**, 3060 (1975).
[32]H. Muramatsu, T. Miura, H. Nakahara, M. Fujioka, E. Tanaka, and A. Hashizume, Hyp. Int. **20**, 305 (1984), and references cited therein.